Notes on Numerical Fluid Mechanics

Volume 68

Recent Development of Aerodynamic Design Methodologies

Inverse Design and Optimization

Edited by

Kozo Fujii and

George S. Dulikravich

A chapter in *Recent Development of Aerodynamic Design Methodologies - Inverse Design and Optimization*,
Fujii, K. and Dulikravich, G. S. (Editors):
Vieweg Series on ***Notes on Numerical Fluid Mechanics***, Springer, 1998.

Using Existing Flow-Field Analysis Codes for Inverse Design of Three-dimensional Aerodynamic Shapes

George S. Dulikravich and Daniel P. Baker

Department of Aerospace Engineering
The Pennsylvania State University, University Park, PA 16802, U.S.A.
e-mail: ft7@psu.edu

Abstract

This chapter demonstrates that it is possible to use existing proven arbitrary flow-field analysis codes without any modifications to perform inverse aerodynamic design of two-dimensional and three-dimensional shapes. A general concept for inverse design of aerodynamic shapes based on treating the aerodynamic surface as an elastic membrane subject to a specified surface pressure distribution is explained. A new mathematical formulation based on the Fourier series analytical solution of this model is detailed. The method is formulated for two-dimensional and for three-dimensional configurations. It can be used in conjunction with any available flow-field analysis code without a need for modification of such a code. Preliminary testing of the new method is performed with a potential flow surface panel code, an Euler flow solver, and a Navier-Stokes flow solver. The convergence rate of the design process is found to be similar for both non-lifting and lifting aerodynamic shapes with the Navier-Stokes flow solver typically requiring minimum number of design iterations. Suggestions for further research and improvements are made.

Introduction

Aerodynamic shape inverse design methods have the goal of determining the proper shape of aerodynamic body such that a desired (target) pressure distribution is achieved on its surface. There are several methods [1,2,3] that are capable of such inverse determination of domain size and shape, but most of the methods require the development of new complex mathematical formulations and the accompanying new software. The majority of inverse design methods require at least the modification of boundary conditions enforcement subroutines. This is often non-trivial and even impossible to do if the source code is not available to the designer. Therefore, inverse shape design methods that require a minimum of software development and can accept any existing reliable flow-field analysis computer code as a large interchangeable subroutine are highly desirable.

This chapter focuses on one such formulation. The so-called elastic surface membrane concept was first proposed by Garabedian and McFadden [4,5] who considered the surface of an aerodynamic body to deform under aerodynamic loads in a manner similar to an elastic membrane. Their method was then adapted by Malone et al. [6-9] into what is presently

known as the MGM (modified Garabedian-McFadden or Malone-Garabedian-McFadden) technique.

The idea behind this method is to model the boundary of an aerodynamic body as a thin elastic membrane. The membrane is then subjected to a distributed normal forcing function represented by the local differences between target (specified) surface coefficients of pressure and those surface coefficients of pressure found by performing an aerodynamic flow-field analysis of the guessed body shape. Due to the membrane's elasticity, it then iteratively and smoothly deforms with time until reaching a steady state configuration, whereby the target pressure values are matched by those generated by the deformed shape. To model the damped, unsteady motion of the elastic surface, any artificial or non-physical governing equation can be used, relating local membrane deformations to the distribution of the forcing function on the surface of the membrane. One such model, as suggested by Garabedian and McFadden [4,5], is

$$\beta_0 \frac{\partial \Delta n}{\partial \tau} + \beta_1 \frac{\partial^2 \Delta n}{\partial x \partial \tau} + \beta_2 \frac{\partial^3 \Delta n}{\partial x^2 \partial \tau} = \Delta C_p \tag{1}$$

Here, Δn is the local outward normal deformation of the airfoil contour, τ is the time coordinate, x is the Cartesian spatial coordinate, while coefficients β are user specified and of order one. The local difference between the target and the actual computed surface coefficients of pressure is

$$\Delta C_p = C_{p\ target} - C_{p\ actual} \tag{2}$$

Since the objective is to determine the steady state condition of the aerodynamic forces, the time derivatives in Eq. (1) can be eliminated by discretizing the artificial time into equal steps corresponding to each iteration of the inverse design procedure. If these iterative time steps are treated as $\Delta\tau = 1$, then Eq. (1) becomes an ordinary differential equation with constant coefficients and a forcing function

$$\beta_0 \Delta n + \beta_1 \frac{d\Delta n}{dx} + \beta_2 \frac{d^2 \Delta n}{dx^2} = \Delta C_p \tag{3}$$

A common modification to the shape evolution equation (3) is to allow deformations to occur only in the Cartesian y-direction, simplifying the update of geometries and allowing for faster computation. This approach, as used by Malone, assumes the governing equation

$$\beta_0 \Delta y + \beta_1 \frac{d\Delta y}{dx} + \beta_2 \frac{d^2 \Delta y}{dx^2} = \Delta C_p \tag{4}$$

Traditionally, Eq. (4) is solved for the correction (Δy) in airfoil y-coordinates by discretizing the airfoil contour and utilizing finite differencing at each discretization point, i, on that contour to represent the first derivative and the second derivative in Eq. (4). After finite differencing at all of the surface membrane points, the result is a set of linear algebraic equations of the form

$$a_i \Delta y_{i-1} + b_i \Delta y_i + c_i \Delta y_{i+1} = \Delta C_{p_i} \tag{5}$$

In the general case when the contour discretization points are unevenly spaced, the finite difference formulas applied at any point on the airfoil upper contour result in

$$a_i = \frac{\beta_1}{x_i - x_{i-1}} - \frac{2\beta_2}{(x_i - x_{i-1})(x_{i+1} - x_{i-1})} \tag{6}$$

$$b_i = -\beta_0 - \frac{\beta_1}{x_k - x_{k-1}} - \frac{\beta_2}{(x_k - x_{k-1})(x_{k+1} - x_k)} \tag{7}$$

$$c_i = -\frac{2\beta_2}{(x_{i+1} - x_{i-1})(x_{i+1} - x_i)} \tag{8}$$

while on the airfoil lower contour the result is

$$a_i = \frac{2\beta_2}{(x_{i+1} - x_{i-1})(x_i - x_{i-1})} \tag{9}$$

$$b_i = \beta_0 - \frac{\beta_1}{x_{i+1} - x_i} - \frac{\beta_2}{(x_i - x_{i-1})(x_{i+1} - x_i)} \tag{10}$$

$$c_i = \frac{\beta_1}{x_{i+1} - x_i} - \frac{2\beta_2}{(x_{i+1} - x_i)(x_{i+1} - x_{i-1})} \tag{11}$$

The tri-diagonal system (Eq. 5) can easily and efficiently be solved using the Thomas algorithm. To avoid the ambiguity of the upper and lower contour finite difference equations, one approach is to fix the trailing edge point.

$$\Delta y_{TE} = 0 \tag{12}$$

and to make the motion of the leading edge node as the average of the displacements of the two nodes adjacent to it

$$\Delta y_{\text{leading edge}} = \frac{\Delta y_{\text{leading edge-1}} + \Delta y_{\text{leading edge+1}}}{2} \tag{13}$$

One major problem with the classical MGM approach is its slow convergence at the leading and trailing edges of the airfoil, as compared to the mid-chord regions of the airfoil. Another major problem is the governing equation's non-physical, *ad hoc* nature. Furthermore, there is no analytical method to determine the optimum coefficients β_0, β_1, β_2 in Eq. (4), although their choice can radically change the convergence of the MGM inverse shape design process.

In order to improve the quality of the solution of Eq. (4), higher order accurate finite difference schemes can be implemented by increasing the stencil size used in the calculation of the derivatives of y-coordinate corrections. This is most easily done by rediscretizing the airfoil surface such that equidistant points along the airfoil surface contour are used. Unfortunately, all benefits of grid clustering are lost in the process. Because the stencil size

for all derivatives is increased with improved order of accuracy, stencils for derivatives at points near the leading and trailing edges of the airfoil can then be made to wrap around to the other side of the airfoil. This also aids to the smoothness of leading and trailing edge deformation. In general, the more neighboring points used in the determination of derivatives at each grid index, the more accurate the derivative. However, the effects of increasing the derivative order of accuracy are negligible or even detrimental once a certain order of accuracy has been reached. From numerical experimentation, the optimum stencil size in most cases was found to be five. When more than five points are used in the determination of derivatives in Eq. (4), all benefits of increased order of accuracy are opposed by errors caused by numerical singularity in the coefficient matrix. A disadvantage of larger stencil size is that the coefficient matrix multiplying the nodal displacements is no longer tri-diagonal, and must be inverted in a more computationally intensive manner. Using a singular value decomposition algorithm [10] to invert the matrix and minimize the effect of singularities (which occur with higher frequency as the derivative order of accuracy is increased) requires a number of computations proportional to the cube of the number of surface nodes. In comparison, tri-diagonal systems of equations can be solved with calculations on the order of the number of equations to the first power. Thus, the higher order accurate process is significantly slower per iteration than the traditional MGM approach.

In an attempt to counter these problems while improving the convergence rate of the design process, a new method of solution of the elastic membrane equation has been devised [11,12]. It is based on the transformation of the derivatives with respect to x-coordinate in Eq. (4) to derivatives with respect to airfoil contour-following coordinate, s. This method uses an analytical solution of the shape evolution equation in terms of a Fourier series.

Fourier Series Solution of the Two-dimensional Shape Evolution Equation

The analytical solution of the MGM equation given in Eq. (4) is complicated by the fact that the β_0 and β_2 terms switch signs when moving from the bottom surface of the airfoil to the top surface (or vice versa). If β_0, β_1, β_2 are considered to be positive constants, Eq. (4) takes the following forms on the top and bottom surfaces of an airfoil:

Top Surface:
$$\beta_0 \Delta y + \beta_1 \frac{d\Delta y}{ds} - \beta_2 \frac{d^2 \Delta y}{ds^2} = \Delta C_p(s) \tag{14}$$

Bottom Surface:
$$-\beta_0 \Delta y + \beta_1 \frac{d\Delta y}{ds} + \beta_2 \frac{d^2 \Delta y}{ds^2} = \Delta C_p(s) \tag{15}$$

Both of these equations can be considered as the generalized mass-damper-spring equation.

$$k\Delta y + c\frac{\partial \Delta y}{\partial s} + m\frac{\partial^2 \Delta y}{\partial s^2} = \Delta C_p \tag{16}$$

Here, the time coordinate has been replaced with the surface following coordinate, s, and the forcing function $\Delta C_p(s)$ is an arbitrary function of the coordinate s. The homogeneous solution of Eq. (16) can be found by assuming

$$\Delta y_h = e^{\lambda s} \tag{17}$$

On the bottom surface of the airfoil

$$k^{bottom} = \beta_0 \tag{18}$$

$$c = \beta_1 \tag{19}$$

$$m^{bottom} = -\beta_2 \tag{20}$$

This leads to

$$\lambda_{1,2}^{bottom} = \frac{-\beta_1 \pm \sqrt{\beta_1^{\,2} + 4\beta_0\beta_2}}{-2\beta_2} \tag{21}$$

$$\Delta y_h^{bottom} = F^{bottom} e^{\lambda_1^{bottom} s} + G^{bottom} e^{\lambda_2^{bottom} s} \tag{22}$$

On the top surface of the airfoil, the signs of k and m reverse

$$k^{top} = -\beta_0 \tag{23}$$

$$m^{top} = \beta_2 \tag{24}$$

This leads to

$$\lambda_{1,2}^{top} = \frac{-\beta_1 \pm \sqrt{\beta_1^{\,2} + 4\beta_0\beta_2}}{2\beta_2} \tag{25}$$

$$\Delta y_h^{top} = F^{top} e^{\lambda_1^{top} s} + G^{top} e^{\lambda_2^{top} s} \tag{26}$$

where F and G are (as yet) undetermined coefficients. The particular solution of Eq. (16) can be found by creating a Fourier series expansion of the function $\Delta C_p(s)$

$$\Delta C_p(s) = a_0 + \sum_n \left[a_n \cos N_n s + b_n \sin N_n s\right] \tag{27}$$

where

$$N_n = \frac{n\pi}{L} \tag{28}$$

Here, L is one-half of the total arc length of the airfoil contour. A particular solution is assumed of the form

$$\Delta y_p = A_0 + \sum_{n=1}^{\infty}[A_n \cos N_n s + B_n \sin N_n s] \tag{29}$$

$$\frac{\partial \Delta y_p}{\partial s} = \sum_{n=1}^{\infty}[-A_n N_n \cos N_n s + B_n N_n \sin N_n s] \tag{30}$$

$$\frac{\partial^2 \Delta y_p}{\partial s^2} = -\sum_{n=1}^{\infty}[A_n N_n^2 \cos N_n s + B_n N_n^2 \sin N_n s] \tag{31}$$

Substitution of Eq. (27) and Eqs. (29-31) into the general evolution equation (16) and collection of like terms yields

$$A_0 = \frac{a_0}{k} \tag{32}$$

$$A_n = \frac{a_n(k - N_n^2 m) - b_n(cN_n)}{(k - N_n^2 m)^2 + (cN_n)^2}, n = 1,2,3,\cdots \tag{33}$$

$$B_n = \frac{b_n(k - N_n^2 m) + a_n(cN_n)}{(k - N_n^2 m)^2 + (cN_n)^2}, n = 1,2,3,\cdots \tag{34}$$

Thus, the complete solution for Δy on the top and bottom surface of the airfoil is

$$\Delta y = Fe^{\lambda_1 s} + Ge^{\lambda_2 s} + A_0 + \sum_{n=1}^{\infty}[A_n \cos N_n s + B_n \sin N_n s] \tag{35}$$

The unknown constants, F and G, on the top and bottom surfaces are determined by specifying four boundary conditions. The following four conditions can be used: trailing edge closure, leading edge closure, zero trailing edge displacement, and smoothness of Δy at the leading edge. For trailing edge closure condition can be expressed as

$$\Delta y^{bottom}(0) = \Delta y^{top}(2L) \tag{36}$$

For pinned trailing edge,

$$\Delta y^{bottom}(0) = 0 \tag{37}$$

The combination of Eq. (35) and Eq. (36) yields the following boundary condition equation

$$F^{bottom} + G^{bottom} = -\sum_{n=0}^{\infty} A_n^{bottom} \tag{38}$$

Similarly, the combination of Eq. (35) and Eq. (37) yields the following boundary condition equation

$$F^{top} e^{2L\lambda_1^{top}} + G^{top} e^{2L\lambda_2^{top}} = -\sum_{n=0}^{\infty} A_n^{top} \tag{39}$$

The leading edge closure condition

$$\Delta y^{bottom}(s_{LE}) = \Delta y^{top}(s_{LE}) \tag{40}$$

can be expressed as

$$\begin{aligned} F^{bottom} e^{s_{LE}\lambda_1^{bottom}} + G^{bottom} e^{s_{LE}\lambda_2^{bottom}} - F^{top} e^{s_{LE}\lambda_1^{top}} - G^{top} e^{s_{LE}\lambda_2^{top}} \\ = \Delta y_p^{top}(s_{LE}) - \Delta y_p^{bottom}(s_{LE}) \end{aligned} \tag{41}$$

The smooth leading edge deformation condition

$$\frac{d}{ds}\Delta y^{bottom}(s_{LE}) = \frac{d}{ds}\Delta y^{top}(s_{LE}) \tag{42}$$

can be expressed as

$$\begin{aligned} & F^{bottom}\lambda_1^{bottom} e^{s_{LE}\lambda_1^{bottom}} + \lambda_2^{bottom} G^{bottom} e^{s_{LE}\lambda_2^{bottom}} \\ & - F^{top}\lambda_1^{top} e^{s_{LE}\lambda_1^{top}} - G^{top}\lambda_2^{bottom} e^{s_{LE}\lambda_2^{top}} \\ & = \frac{d}{ds}\Delta y_p^{top}(s_{LE}) - \frac{d}{ds}\Delta y_p^{bottom}(s_{LE}) \end{aligned} \tag{43}$$

F and G coefficients can be found by simultaneous solution of Eqs. (38, 39, 41, 43).

$$\begin{Bmatrix} F^{bottom} \\ G^{bottom} \\ F^{top} \\ G^{top} \end{Bmatrix} = \begin{bmatrix} 1 & 1 & 0 & 0 \\ 0 & 0 & e^{2L\lambda_1^{top}} & e^{2L\lambda_2^{top}} \\ e^{s_{LE}\lambda_1^{bottom}} & e^{s_{LE}\lambda_2^{bottom}} & -e^{s_{LE}\lambda_1^{top}} & -e^{s_{LE}\lambda_2^{top}} \\ \lambda_1^{bottom} e^{s_{LE}\lambda_1^{bottom}} & \lambda_2^{bottom} e^{s_{LE}\lambda_2^{bottom}} & -\lambda_1^{top} e^{s_{LE}\lambda_1^{top}} & -\lambda_2^{top} e^{s_{LE}\lambda_2^{top}} \end{bmatrix}^{-1} \cdot$$

$$\begin{Bmatrix} -\sum_{n=0}^{\infty} A_n^{bottom} \\ -\sum_{n=0}^{\infty} A_n^{top} \\ \Delta y_p^{top}{}'(s_{LE}) - \Delta y_p^{bottom}{}'(s_{LE}) \\ \Delta y_p^{top}{}'(s_{LE}) - \Delta y_p^{bottom}{}'(s_{LE}) \end{Bmatrix} \tag{44}$$

Since the Fourier series formulation is exact, any errors due to finite differencing and the need for Eq. (13) are removed. The choice of number of Fourier series terms effectively enforces an upper limit on the frequency allowed in the y-coordinate deformation.

Solving the Three-dimensional Shape Evolution Equation

Generalization of the elastic membrane formulation to surfaces of three-dimensional objects can be accomplished by a complete form of a second order partial differential equation of the following type [12]

$$a\frac{\partial^2 \Delta y}{\partial t^2} + b\frac{\partial^2 \Delta y}{\partial s \partial t} + c\frac{\partial^2 \Delta y}{\partial s^2} + d\frac{\partial \Delta y}{\partial s} + e\frac{\partial \Delta y}{\partial t} - f\Delta y = F(\Delta C_p) \tag{45}$$

Here, s and t are the surface coordinates in the general streamwise and spanwise directions, respectively. The forcing function can be generalized as

$$F(\Delta C_p) = \Delta C_p + \alpha_1 \frac{\partial \Delta C_p}{\partial s} + \beta_1 \frac{\partial \Delta C_p}{\partial t} + \alpha_2 \frac{\partial^2 \Delta C_p}{\partial s^2} + \beta_2 \frac{\partial^2 \Delta C_p}{\partial t^2} \tag{46}$$

Here, the coefficients a, b, c, d, e, f, α and β are user specified. The coefficients have been found [4-9, 11,12] to influence the convergence rate of the iterative shape design process. The general variation of the surface forcing function, F, can be represented as a Fourier series

$$F(C_p) = \sum_{n=0}^{n_{max}} \sum_{m=0}^{m_{max}} [A_{mn}\cos(ns)\cos(mt) + B_{mn}\cos(ns)\sin(mt) + C_{mn}\sin(ns)\cos(mt) + D_{mn}\sin(ns)\sin(mt)] \tag{47}$$

Similarly, the particular solution of the elastic membrane equation (45) can be represented in a Fourier series form as

$$\Delta y^p = \sum_{n=0}^{n_{max}} \sum_{m=0}^{m_{max}} [a_{mn}\cos(ns)\cos(mt) + b_{mn}\cos(ns)\sin(mt) + c_{mn}\sin(ns)\cos(mt) + d_{mn}\sin(ns)\sin(mt)] \tag{48}$$

If the mixed second spatial derivative is kept in the general elastic membrane motion equation (45), the homogeneous part of the solution of this equation cannot be found directly. A linear transformation of coordinates [12] is needed in this case that somewhat complicates the process. For the sake of simplicity and the clarity of explanation, we will continue this elaboration with the simplified Eq. (45) and Eq. (46) by working with the assumption that

$$b = \alpha_1 = \beta_1 = \alpha_2 = \beta_2 = 0 \tag{49}$$

These terms can be omitted without any detrimental effects on the robustness and the accuracy of the entire design concept, but they may influence convergence rate of the iterative design process. Then, from Eq. (48) it follows that

$$\frac{\partial \Delta y^p}{\partial s} = \sum_{n=0}^{n_{max}} \sum_{m=0}^{m_{max}} - n[a_{mn} \sin(ns)\cos(mt) + b_{mn} \sin(ns)\sin(mt)$$

$$- c_{mn} \cos(ns)\cos(mt) - d_{mn} \cos(ns)\sin(mt)] \tag{50}$$

$$\frac{\partial^2 \Delta y^p}{\partial s^2} = \sum_{n=0}^{n_{max}} \sum_{m=0}^{m_{max}} - n^2[a_{mn} \cos(ns)\cos(mt) + b_{mn} \cos(ns)\sin(mt)$$

$$+ c_{mn} \sin(ns)\cos(mt) + d_{mn} \sin(ns)\sin(mt)] \tag{51}$$

$$\frac{\partial \Delta y^p}{\partial t} = \sum_{n=0}^{n_{max}} \sum_{m=0}^{m_{max}} - m[a_{mn} \cos(ns)\sin(mt) - b_{mn} \cos(ns)\cos(mt)$$

$$+ c_{mn} \sin(ns)\sin(mt) - d_{mn} \sin(ns)\cos(mt)] \tag{52}$$

$$\frac{\partial^2 \Delta y^p}{\partial t^2} = \sum_{n=0}^{n_{max}} \sum_{m=0}^{m_{max}} - m^2[a_{mn} \cos(ns)\cos(mt) + b_{mn} \cos(ns)\sin(mt)$$

$$+ c_{mn} \sin(ns)\cos(mt) + d_{mn} \sin(ns)\sin(mt)] \tag{53}$$

After substitution of Eqs. (47-53) into Eq. (45) and matching of coefficients multiplying each of the four products of Sine and Cosine functions, the coefficients in Eq. (45) can be expressed as analytical functions of the coefficients in Eq. (46). That is,

$$\begin{bmatrix} \left(-an^2 - cm^2 - f\right) & em & dn & 0 \\ -em & \left(-an^2 - cm^2 - f\right) & 0 & dn \\ -dn & 0 & \left(-an^2 - cm^2 - f\right) & -em \\ 0 & dn & -em & \left(-an^2 - cm^2 - f\right) \end{bmatrix} \begin{Bmatrix} a_{mn} \\ b_{mn} \\ c_{mn} \\ d_{mn} \end{Bmatrix}$$

$$= \begin{Bmatrix} A_{mn} \\ B_{mn} \\ C_{mn} \\ D_{mn} \end{Bmatrix} \tag{54}$$

Thus, the particular solution of Eq. (45) can be found in terms of the coefficients $A_{mn}, B_{mn}, C_{mn}, D_{mn}$ defining the pressure forcing function distribution on the surface of the elastic membrane.

If, in addition to the simplifications listed in Eq. (49), we further simplify the model by using

$$d = e = 0 \tag{55}$$

then the elastic membrane equation reduces to a very simple model given by Eq. (56)

$$a\frac{\partial^2 \Delta y}{\partial s^2} + c\frac{\partial^2 \Delta y}{\partial t^2} - f\Delta y = \Delta C_p \tag{56}$$

The particular solution of Eq. (56) can be expressed as

$$\Delta y^p = \sum_{n=0}^{n_{max}} \sum_{m=0}^{m_{max}} \{[-A_{mn}\cos(ns)\cos(mt) - B_{mn}\cos(ns)\sin(mt) - C_{mn}\sin(ns)\cos(mt) - D_{mn}\sin(ns)\sin(mt)]/(an^2 + cm^2 + f)\} \tag{57}$$

This simple expression is very easy to program. It is capable of generating three-dimensional wing shapes involving both aerodynamic twist and geometric twist variations. When the difference between the specified and the calculated surface pressure has abrupt variations as in the case of a shock wave, this formulation creates a surface depression underneath the shock that oscillates along the wing surface as an undamped surface wave. Consequently, for design of shocked transonic configurations, the simplifications listed in Eq. (54) should not be used.

Inverse Design of a Rectangular Patch of the Surface

If it is desirable to modify only one portion of an aerodynamic surface while maintaining the original shape of the rest of the body, the following formulation should be applied.

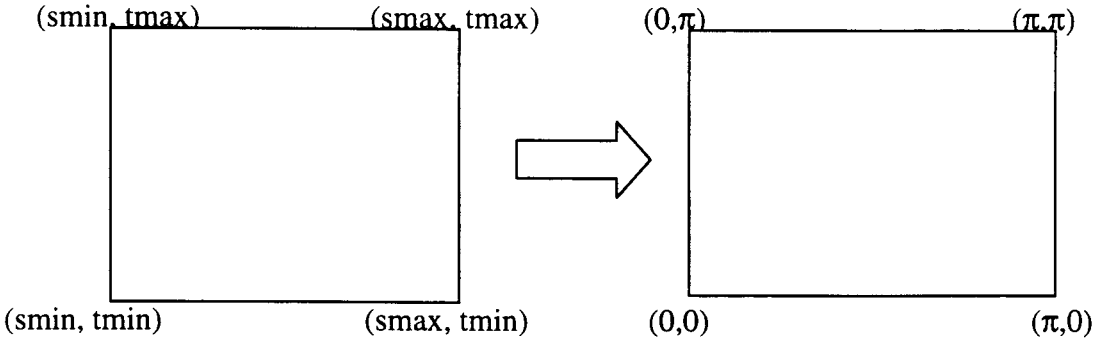

Fig. 1: Coordinate Mapping for Design of a Quadrilateral Surface Patch.

In order to maintain continuity of the surface, Δy at each patch boundary must be fixed at zero. This can be accomplished by scaling the patch s and t coordinates to a rectangle with coordinates as shown in Fig 1, and using a Fourier Sine series (that is, a_{mn}, b_{mn}, c_{mn} =0) to represent the deformation function $\Delta y_p(s,t)$. Then, the particular solution automatically satisfies all boundary conditions, and there is no need for a homogeneous solution.

$$\Delta y(s,t) = \sum_{n=1}^{n_{max}} \sum_{m=1}^{m_{max}} \frac{-D_{mn}\sin(ns)\sin(mt)}{an^2 + cm^2 + f} \tag{58}$$

Inverse Design of Three-dimensional Wings

For wing shape design it is desirable to enforce the following boundary conditions on the displacement Δy:

1. The displacement should be symmetric about the root section (vertical symmetry plane).
2. The displacement should be periodic in the s-direction for each span station.
3. The span-wise derivative of the displacement should be zero at the root section.
4. One point should be fixed. For example, the trailing edge of the root section can be fixed.

Firstly, scaling of the s and t coordinates of the wing should be performed as shown in Fig. 2.

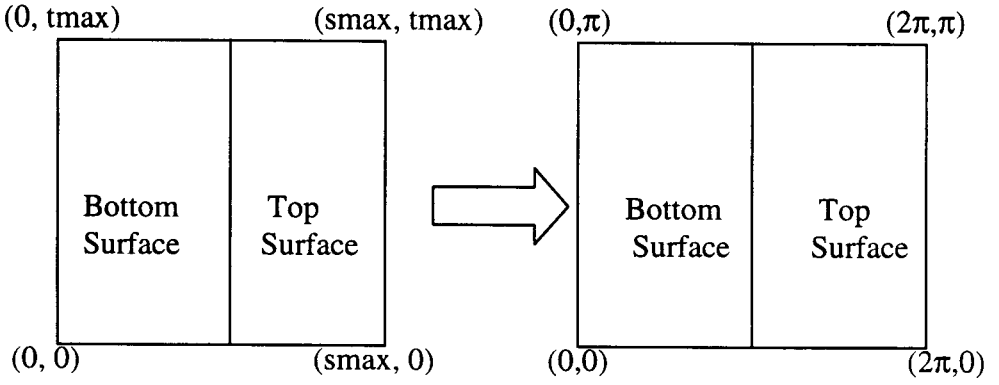

Fig. 2: Coordinate Mapping for Design of a Three-dimensional Wing.

Then, the four above boundary conditions can be mathematically expressed as:

$$\Delta y(s,t) = \Delta y(s,-t) \tag{59}$$

$$\Delta y(0,t) = \Delta y(2\pi n,t) \tag{60}$$

$$\Delta y_t(s,0) = 0 \tag{61}$$

$$\Delta y(0,0) = 0 \tag{62}$$

A Cosine series in the t-direction with Sine and Cosine terms in the s-direction for the particular solution with assumptions listed in Eq. (49) and Eq. (55) automatically satisfies the first three boundary conditions.

$$\Delta y^p(s,t) = \sum_{n=0}^{n_{max}} \sum_{m=0}^{m_{max}} \frac{-A_{mn}\cos(ns)\cos(mt) - C_{mn}\sin(ns)\cos(mt)}{an^2 + cm^2 + f} \tag{63}$$

Using a solution of the homogeneous part of the simplified elastic membrane equation can satisfy the remaining boundary conditionIf Δy^h is a function of coordinate t only, the solution can be expressed as

$$\Delta y^h = F\cosh t\sqrt{\frac{f}{a}} + G\sinh t\sqrt{\frac{f}{a}} \tag{64}$$

For zero displacement at the wing root trailing edge point,

$$\Delta y^h(0) = -\Delta y^p(0,0) = \sum_{n=0}^{n_{max}} \sum_{m=0}^{m_{max}} \frac{A_{mn}}{an^2 + cm^2 + f} \tag{65}$$

$$\Delta y^h(0) = F \tag{66}$$

$$F = \sum_{n=0}^{n_{max}} \sum_{m=0}^{m_{max}} \frac{A_{mn}}{an^2 + cm^2 + f} \tag{67}$$

For zero slope of displacement in the t-direction at the root,

$$\frac{\partial \Delta y^h}{\partial t}(0) = -\frac{\partial \Delta y^p}{\partial t}(0,0) = 0 \tag{68}$$

$$\frac{\partial \Delta y^h}{\partial t} = (F \sinh t\sqrt{\frac{f}{a}} + G \cosh t\sqrt{\frac{f}{a}})\sqrt{\frac{f}{a}} \tag{69}$$

$$\frac{\partial \Delta y^h}{\partial t}(0) = G\sqrt{\frac{f}{a}} \tag{70}$$

$$G = 0 \tag{71}$$

$$\Delta y^h = \sum_{n=0}^{n_{max}} \sum_{m=0}^{m_{max}} \frac{A_{mn} \cosh\left(t\sqrt{\frac{f}{a}}\right)}{an^2 + cm^2 + f} \tag{72}$$

Combining the homogeneous solution (Eq. 72) and particular solution (Eq. 63) results in

$$\Delta y(s,t) = \sum_{n=0}^{n_{max}} \sum_{m=0}^{m_{max}} \frac{A_{mn}[\cosh\left(t\sqrt{\frac{f}{a}}\right) - \cos(ns)\cos(mt)] - C_{mn}\sin(ns)\cos(mt)}{an^2 + cm^2 + f} \tag{73}$$

Numerical Results

a) Two-dimensional airfoils

The high non-linearity of flow-field governing equations, such as Euler and Navier-Stokes equations, has been suspected to cause significant reduction in the speed of MGM convergence [9]. To clarify this issue, three flow-field analysis codes have been used in conjunction with the original MGM and the Fourier series method. The three flow-field analysis codes were: a surface panel code with a compressibility correction, an Euler equation

solution compressible flow code, and a compressible viscous flow Navier-Stokes code with a Baldwin-Lomax turbulence model.

Two airfoil design cases were examined. The first case utilized a target coefficient of pressure distribution corresponding to a NACA0012 non-lifting airfoil at free stream Mach number M = 0.5. The initial geometry in this case was a NACA 0009 non-lifting airfoil. The second case utilized the coefficient of pressure distribution of a NACA1311 cambered airfoil as its target. The initial geometry here was a NACA0012 non-lifting airfoil. In both cases, the inverse design process was performed using each of the three flow-field analysis codes in conjunction with the MGM procedure and the Fourier series technique. Composite plots of the convergence histories of these processes are shown in Fig. 3. For both design cases and all three flow-field analysis codes, the Fourier technique outperformed the MGM technique. A typical geometry and coefficient of pressure distribution evolution using the Fourier technique are shown in Fig. 4.

The slow convergence of the classical MGM technique with nonlinear flow-field analysis codes is most evident in the case of the lifting airfoil design (Fig. 3b). In this case, the Euler + MGM combination ceases to converge after three design iterations, and the Navier-Stokes + MGM combination ceases its convergence after five design iterations. This difficulty was not encountered when using the Fourier series technique, as in both the lifting and non-lifting cases the design converged faster with the Euler and Navier-Stokes analysis codes than with the panel code [11].

b) Three-dimensional wings

Several wing design test cases were carried out using a three-dimensional panel code with an algebraic compressibility correction. The wingtip airfoil in each test case had a non-zero thickness. Each inverse shape design test case was performed with free-stream Mach number M = 0.2. For all three-dimensional results, the maximum number of Fourier terms to be considered in the s- and t-directions, n_{max} and m_{max}, were set to 120.

The first panel case tested the Fourier technique's ability to modify a wing's thickness without affecting its symmetry. The wing planform was rectangular with a semi-span three times as large as the chord. The target pressure distribution was obtained from a three-dimensional panel code analysis of a wing whose airfoil shape varied smoothly from a NACA0012 airfoil at the root section to a NACA0009 airfoil at the wingtip. The initial guess wing had a NACA0012 airfoil shape at all span stations. The wing grid had 64 panels in the s-direction and 19 panels in the spanwise direction. The shape evolution parameters a, c, and f were set to 6.0, 0.5, and 1.5, respectively.

As shown in Figure 5, the designed wing's coefficient of pressure distribution nearly duplicated the target after ten calls to the flow-field analysis code. Small discrepancies in the pressure distribution can be seen at the wing tip section, and there is a noticeable bump in the pressure distribution of each section of the designed wing near the trailing edge. This trailing edge pressure spike, though physically unexplainable, occurred in each of the three-dimensional panel code tests that were performed. The shapes of the initial wing, the final wing, and the wing after one design iteration are shown in Fig. 6. The essential three-dimensionality of the shape change can be most notably seen at 0% span. Here, where the initial and the target airfoil geometries and corresponding pressure distributions are identical,

one would expect no change of the root airfoil shape during the inverse shape design process. However, as the general trend of the entire wing is toward a lower thickness, the root section experiences some loss of thickness after one iteration. The root section must then regain its original shape. Thus, in such a case where the root section coefficient of pressure is unmodified in the design target, it could be quite useful if the entire root section of the wing geometry is kept unchanged. Also, at 30% span, the initial geometry modification overshoots the appropriate thickness of the wing, but then converges to the target shape after approximately ten design iterations.

The second panel test case examined wing twist. The wing planform was rectangular with a semi-span of two chord lengths. The target pressure distribution was calculated from analysis of a wing with NACA0012 airfoil with a one degree angle of attack at the root section and three degrees angle of attack at the tip. The initial guess geometry also had a NACA0012 airfoil shape, but included no wing twist. The wing grid had 64 panels in the s-direction and 14 panels in the spanwise direction, clustered toward the wingtip. Parameters a, c, and f were set to 6.0, 0.5, and 1.5 respectively. Figure 7 depicts the initial coefficient of pressure distributions at several span stations and their values after the tenth iteration with the Fourier series design method, and the target values. Again, a spike in the pressure distribution is being generated at the trailing edge of the wing, most noticeably at 80% of the wing span. Figure 8 depicts the initial geometry and the geometry after the first and the tenth iteration.

The third panel case involved evolving wing thickness, camber, and twist. The wing had a taper ratio of 0.5 and a leading edge backward sweep angle of 7.125 degrees. The semi-span was equal to two root chord lengths. The target pressure distribution was obtained from analysis of a wing having a NACA1311 root airfoil shape and a NACA2412 tip airfoil shape with three degrees angle of attack at the tip. The initial geometry had a constant NACA0009 airfoil shape with a negative one degree angle of attack at the tip. The wing grid had 64 panels in the s-direction and 19 panels in the spanwise direction that were clustered toward the wingtip. The shape evolution parameters a, c, and f were set to 7.0, 0.9, and 1.2. As seen in Fig. 9, the target pressure differs from the tenth iteration design values mostly near the wingtip and at the trailing edge. The evolution of the geometry is shown in Fig. 10.

The fourth test case was examined in conjunction with both a three-dimensional Euler equation solver and a turbulent Navier-Stokes equation solver. In these cases, a wingtip that quickly shrinks the airfoil thickness down to zero was added to each wing. The computational grid was regenerated after each application of the Fourier series design method by stacking two-dimensional C-grids generated for each span station. Additional grid layers were provided beyond the wingtip so that finite wing effects could be included.

The subsonic Euler design case was applied to a wing with a taper ratio of 0.5. The leading edge sweep angle was 14.03 degrees and the trailing edge had zero sweep, while the semi-span was two times the root chord length. The free stream Mach number was M = 0.6. The target pressure distribution corresponded to a severely twisted wing with a root airfoil NACA0009 at +4 degrees angle of attack and a tip airfoil NACA1311 at –4 degrees angle of attack. The initial geometry for the design process had root airfoil NACA2412 at –4 degrees angle of attack and a tip airfoil NACA0009 at +4 degrees angle of attack. Twenty span stations, 32 C-layers, 64 grid cells on each airfoil, and 16 cells along the wake defined the computational grid. The shape evolution parameters a, c, and f were set to 7.0, 0.9, and 1.2, respectively. The preliminary results indicate (Fig. 11) that target pressure distribution is not

fully achieved near the root and tip after twenty design iterations. Figure 12 depicts the change in geometry of the wing during the design process.

The subsonic Navier-Stokes design case was identical to the subsonic Euler case, except that viscosity effects were included in the target pressure distribution. A Reynolds number of one million was used. The shape evolution parameters a, c, and f were set to 7.0, 0.9, and 1.2, respectively. The results of this inverse shape design case are shown in Figs. 13 and 14. Comparison with the results from the corresponding Euler case (Figs. 11 and 12) shows little difference in the performance of the code.

One Euler equation design case was attempted in transonic flight conditions, seeking to design a fully subsonic wing from a wing with a shock wave at the flight Mach number M = 0.8. The wing planform had a taper ratio of 0.5, leading edge sweep angle of 14.03 degrees, zero trailing edge sweep, and semi-span of two times the root chord length. The initial guess had a NACA0012 airfoil shape at 5 degrees angle of attack. The target pressure distribution corresponded to a high subsonic non-lifting wing with a NACA0009 airfoil. The computational grid was defined by 20 span stations, 32 C-layers, and 100 grid cells per airfoil. The shape evolution parameters a, c, and f were set to 7.0, 1.2, and 1.6, respectively. As shown in Fig. 15, after twenty iterations, the wing still had some lift despite its non-lifting target pressure distribution. More dramatic was the airfoil shape obtained after the first iteration of the Fourier series technique. A large dent was developed at the location of the shock wave on the upper surface of the wing (Fig. 16). A potential danger in supplying a discontinuous pressure distribution as the target pressure in the Fourier series method is that the surface curvature can locally overreact to the discontinuity, causing a concavity on the surface of the wing. However, after 20 iterations in this case, the concavity was removed, leaving a smooth wing shape (Fig. 16) and no shock wave (Fig. 17).

Conclusions and Recommendations

A general formulation for the elastic membrane concept in aerodynamic shape inverse design has been explained. Details were given for a finite-difference based MGM method and for a Fourier series based analytical method for its implementation. The main advantage of both design methods is that they can be very easily programmed and used in conjunction with any available flow-field analysis code without a need for modifying such a code. From a detailed sequence of numerical tests of the Fourier series technique as applied to isolated airfoil design, it can be concluded that the convergence rate of this method does not depend on the non-linearity of the flow-field solver used. The Fourier series method was found to consistently converge faster than the MGM method, resulting in fewer calls to the time consuming flow-field analysis code. When applied to three-dimensional wing design, preliminary results show that the Fourier series technique is able to design subsonic wings in conjunction with a panel code, an Euler solver, or a turbulent Navier-Stokes solver. Cases involving shocked initial or target pressure distributions may be subject to overly dramatic changes in curvature in the region of the shock when using the simplified formulation presented here. It is possible that the inclusion of the mixed second partial derivative term and/or the first derivative terms on the left hand side of the elastic membrane shape evolution equation (56) could eliminate this problem by rapidly damping the elastic surface oscillations.

The addition of derivatives of pressure on the right hand side of the general elastic membrane model (Eqs. 45 and 46) could potentially significantly increase the convergence rate of the design process. Another possibility to significantly reduce the number of calls to the flow-field analysis code would be to devise a procedure for optimizing the user specified coefficients in the elastic membrane model equation.

Acknowledgments

The authors would like to express their gratitude for the NASA Graduate Student Research Program Fellowship facilitated and monitored by Dr. John Malone, the National Science Foundation Grant DMI-9522854 monitored by Dr. George A. Hazelrigg, the NASA Lewis Research Center Grant NAG3-1995 facilitated by Dr. John K. Lytle and supervised by Dr. Kestutis Civinskas, and for Lockheed Martin Skunk Works research grant facilitated by Mr. Thomas Oatway and monitored by Dr. Anthony Thornton.

References

[1] Dulikravich, G.S.: Aerodynamic Shape Design and Optimization: Status and Trends, AIAA Journal of Aircraft, Vol. 29, No. 5, pp. 1020-1026 (Nov./Dec. 1992).

[2] Dulikravich, G.S.: Shape Inverse Design and Optimization for Three-Dimensional Aerodynamics, AIAA invited paper 95-0695, AIAA Aerospace Sciences Meeting, Reno, NV, January 9-12 (1995).

[3] Dulikravich, G.S.: Design and Optimization Tools Development, chapters no. 10-15 in New Design Concepts for High Speed Air Transport, (editor: H. Sobieczky), Springer, Wien/New York, 1997, pp. 159-236 (1997).

[4] Garabedian, P. and McFadden, G.: Computational Fluid dynamics of Airfoils and Wings, in Transonic, Shock, and Multidimensional Flows: Advances in Scientific Computing, pp. 1-16, Academic Press (1982).

[5] Garabedian, P. and McFadden, G.: Design of Supercritical Swept Wings, AIAA J., Vol.20, No.3, pp. 289-291 (March 1982).

[6] Malone, J., Vadyak, J. and Sankar, L.N.: A Technique for the Inverse Aerodynamic Design of Nacelles and Wing Configurations, AIAA Journal of Aircraft, Vol. 24, No. 1, pp. 8-9, (January 1987).

[7] Hazarika, N.: An Efficient Inverse Method for the Design of Blended Wing-Body Configurations, Ph.D. Thesis, Aerospace Eng. Dept., Georgia Institute of Technology (June 1988).

[8] Malone, J.B., Narramore, J.C. and Sankar, L.N.: An Efficient Airfoil Design Method Using the Navier-Stokes Equations, in Proceedings of AGARD Specialists' Meeting on Computational Methods for Aerodynamic Design (Inverse) and Optimization, AGARD-CP-463, (editor: J. Slooff), Loen, Norway, May 22-23 (1989).

[9] Malone, J.B., Narramore, J.C. and Sankar, L.N.: An Airfoil Design Method for Viscous Flows, Proceedings of the 15th Southeastern Conference on Theoretical and Applied Mechanics, Vol. XV, pp. 463-470, (editors: S.V. Hanagud, M.P. Kamat, C.E. Ueng), Georgia Institute of Technology, Atlanta, GA (1990).

[10] Press, W.H, Teukolsky, S.A., Vetterling, W.T. and Flannery, B.P.: Numerical Recipes in FORTRAN, The Art of Scientific Computing, 2nd Edition, Cambridge University Press, Cambridge (1986).

[11] Dulikravich, G.S. and Baker, D.P.: Fourier Series Analytical Solution for Inverse Design of Aerodynamic Shapes, Proceedings of International Symposium on Inverse Problems in Engineering Mechanics - ISIP'98 (editors: M. Tanaka and G.S. Dulikravich), Nagano City, Japan, March 24-27, 1998, Elsevier Science, U.K. (1988).

[12] Dulikravich, G.S. and Baker, D.P.: Aerodynamic Shape Inverse Design Using a Fourier Series Method, AIAA paper 99-0185, Aerospace Sciences Meeting, Reno, NV, January 11-14 (1999).

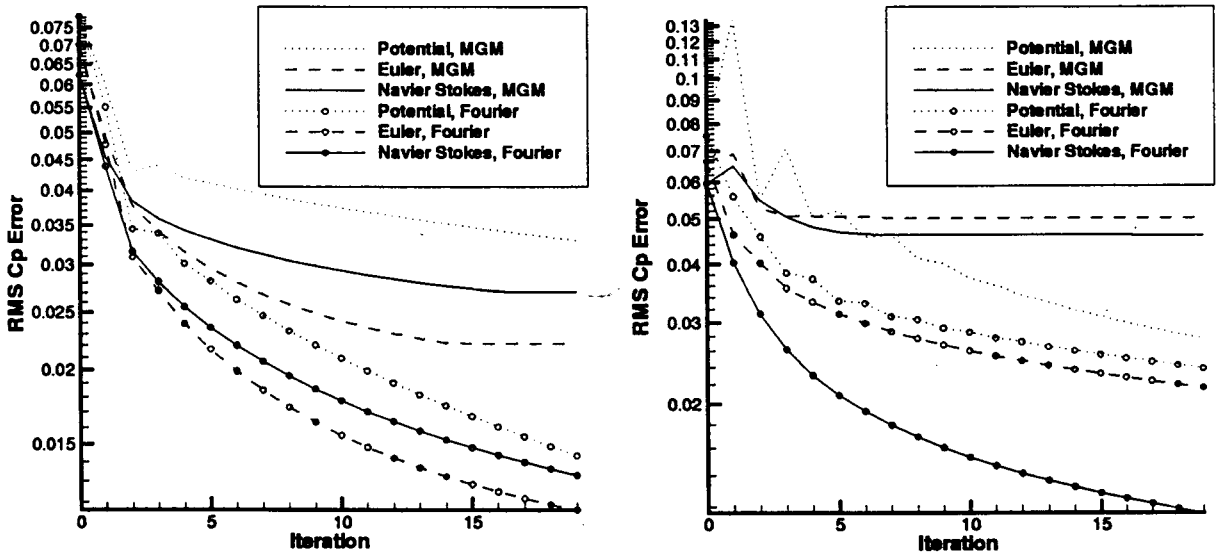

Fig. 3: Convergence histories of MGM and Fourier methods applied to identical problems. M=0.5. Re=1000000 for Navier Stokes case.
(a) Nonlifting case: NACA 0009 evolves into NACA 0012. Beta=(1.2, 0.0, 0.4).
(b) Lifting case: NACA 0012 evolves into NACA 1311. Beta=(1.4, 0.0, 0.6).

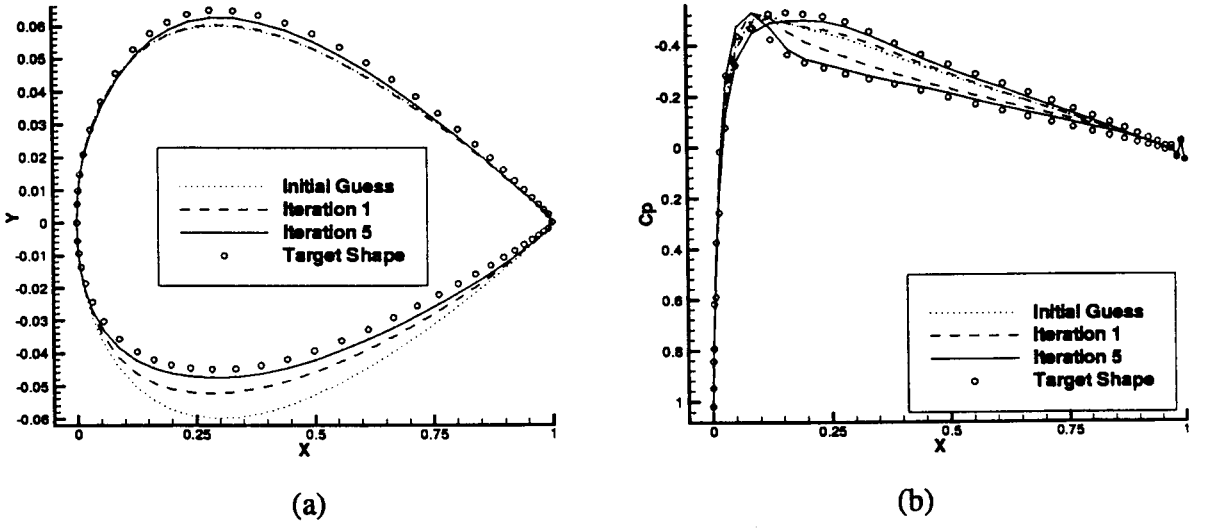

Fig. 4: Fourier method: evolution from NACA 0012 to NACA 1311 airfoil. Navier Stokes solver. M=0.5. Re=1000000. Beta=(1.4, 0.0, 0.6)
(a) Evolution of geometry. Y-axis enlarged for clarity.
(b) Evolution of surface coefficient of pressure.

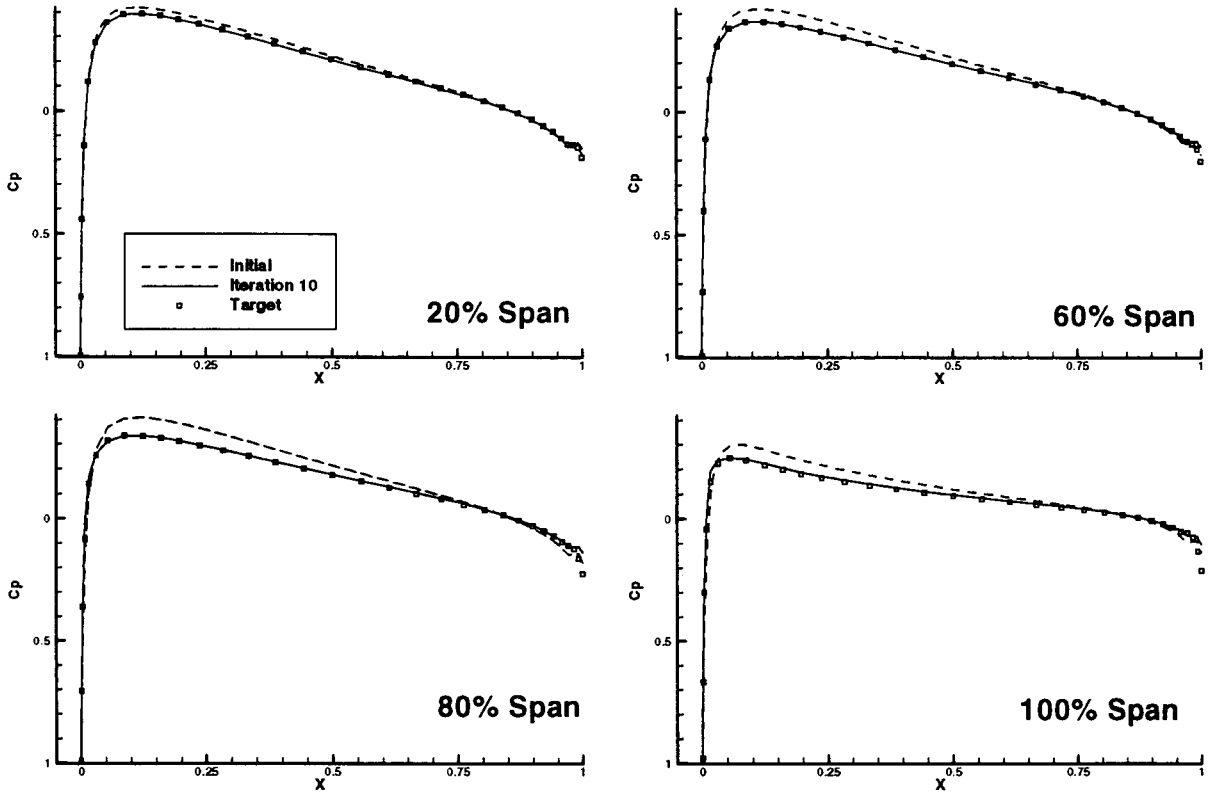

Fig. 5: Sectionwise Cp distributions for panel code symmetric case no. 1

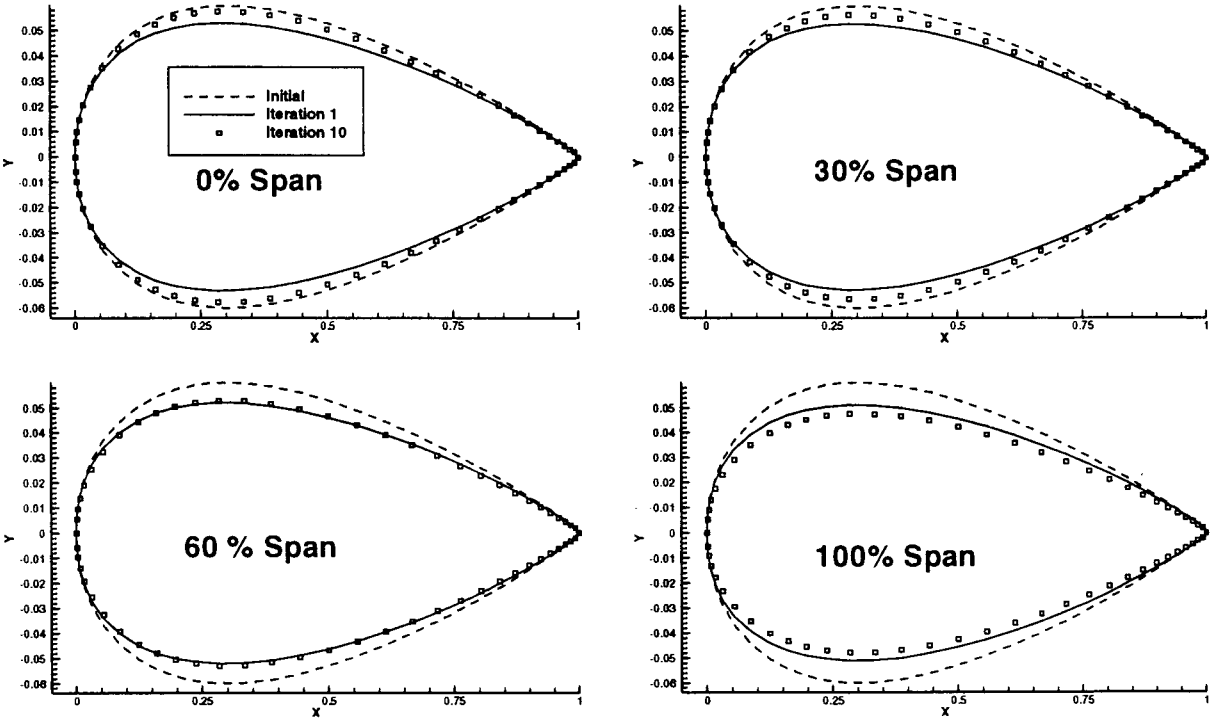

Fig. 6: Geometry evolution by section for symmetric panel code symmetric case no. 1. Y-axis enlarged for clarity.

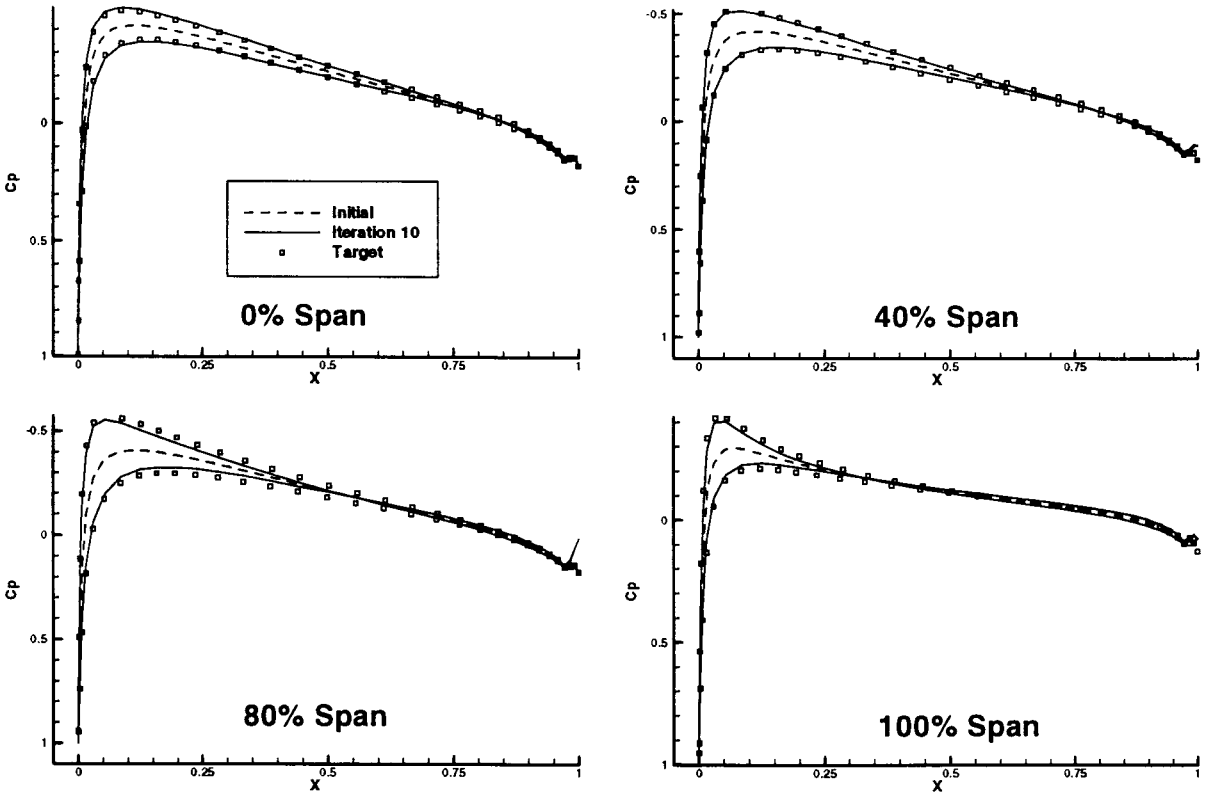

Fig. 7: Sectionwise Cp distributions for panel code twisted case no. 2.

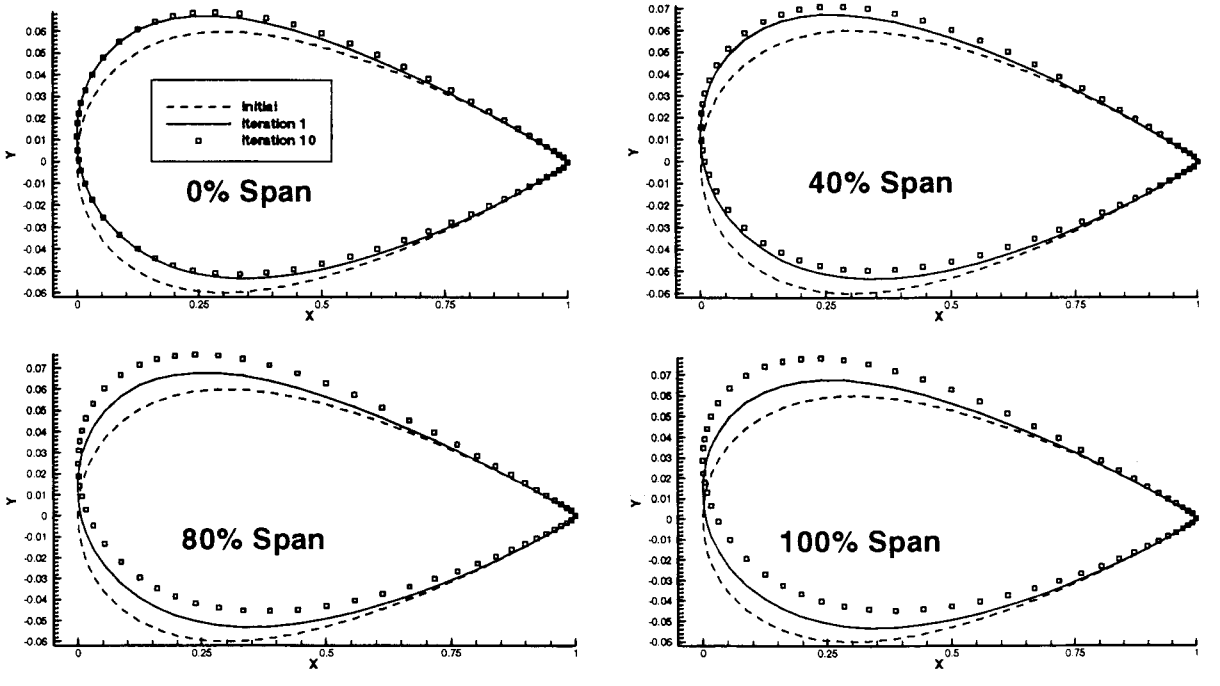

Fig. 8: Geometry evolution by section for panel code twisted case no. 2. Y-axis enlarged for clarity.

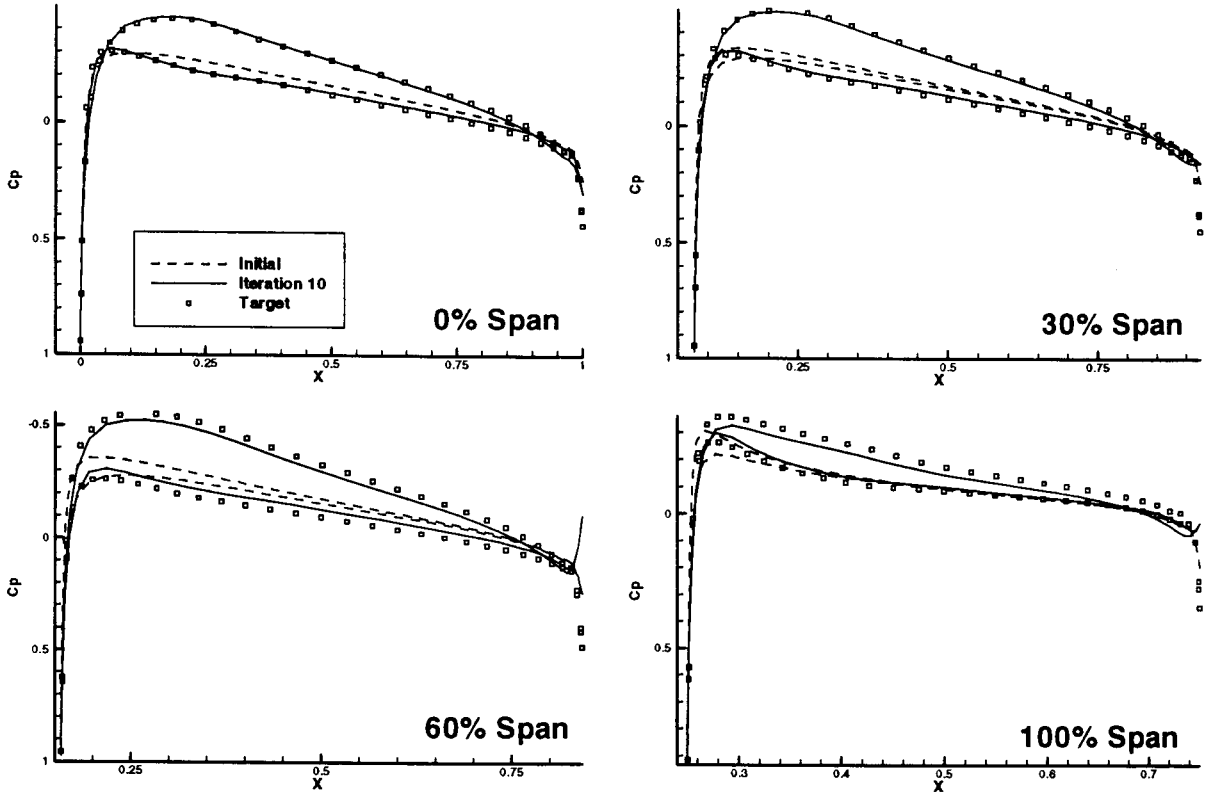

Fig. 9: Sectionwise Cp distributions for panel code lifting case no. 3.

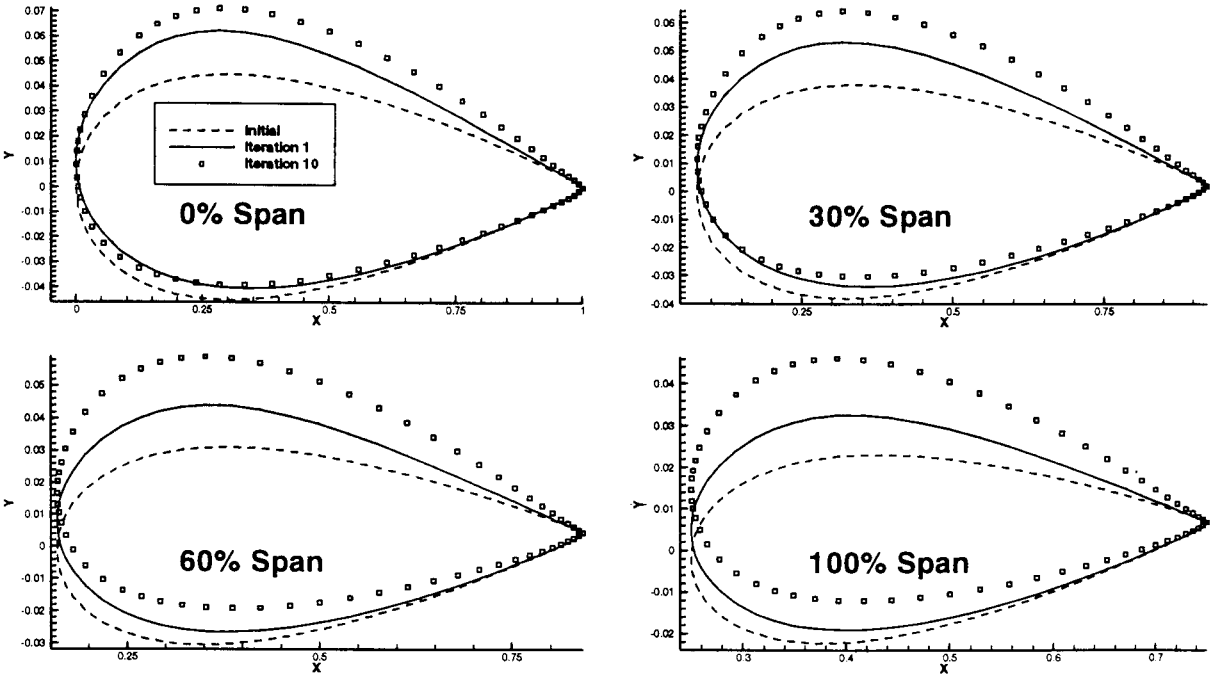

Fig. 10: Geometry evolution by section for panel code lifting case no. 3. Y-axis enlarged for clarity.

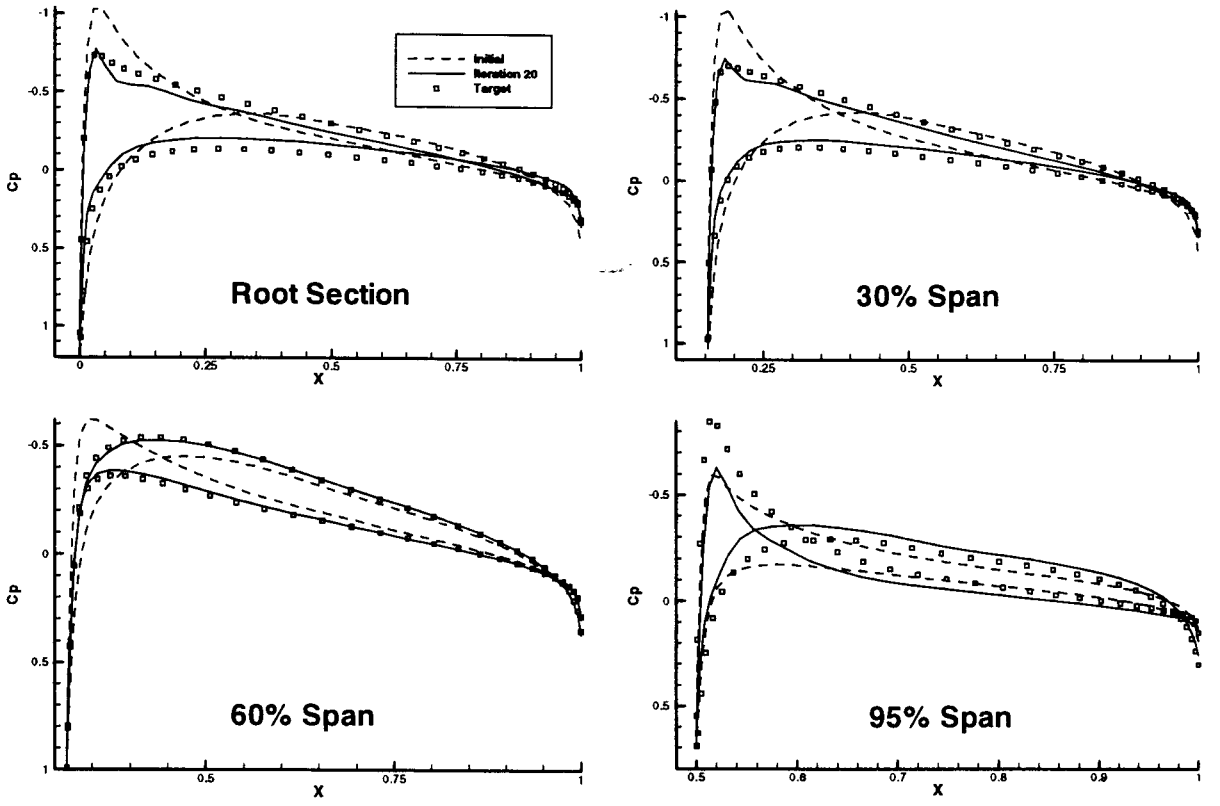

Fig. 11: Sectionwise Cp distributions for severely twisted Euler subsonic case.

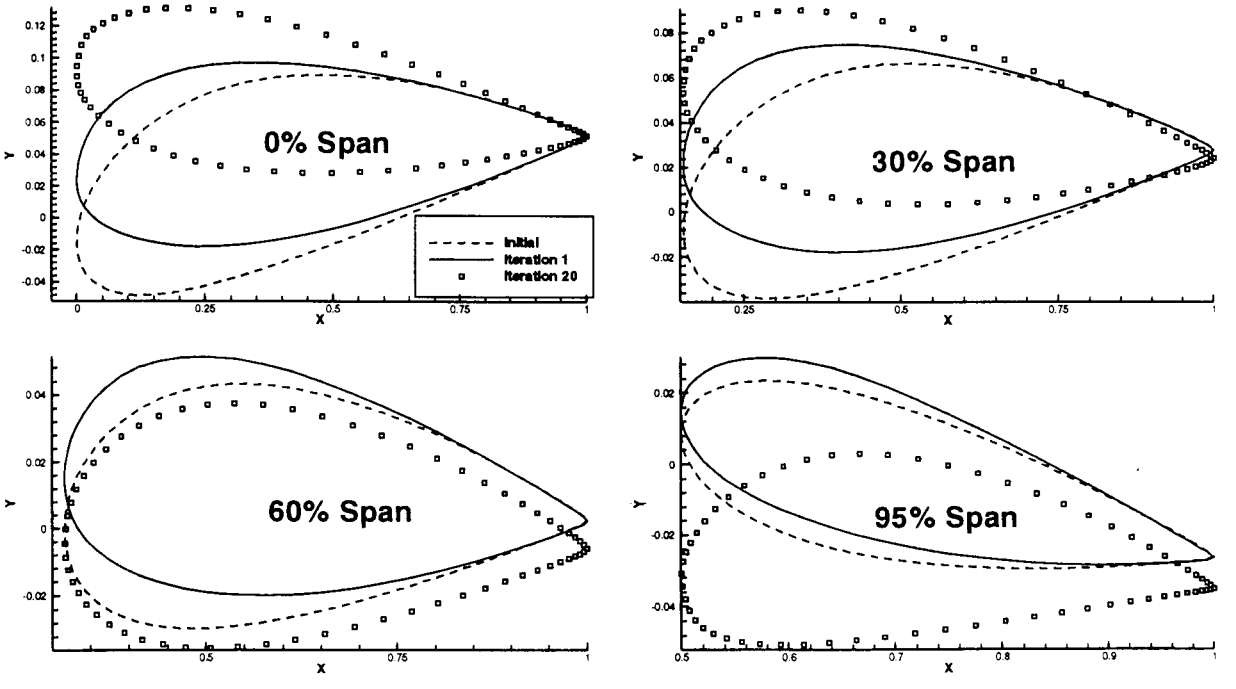

Fig. 12: Geometry evolution by section for severely twisted Euler subsonic case. Y-axis enlarged for clarity.

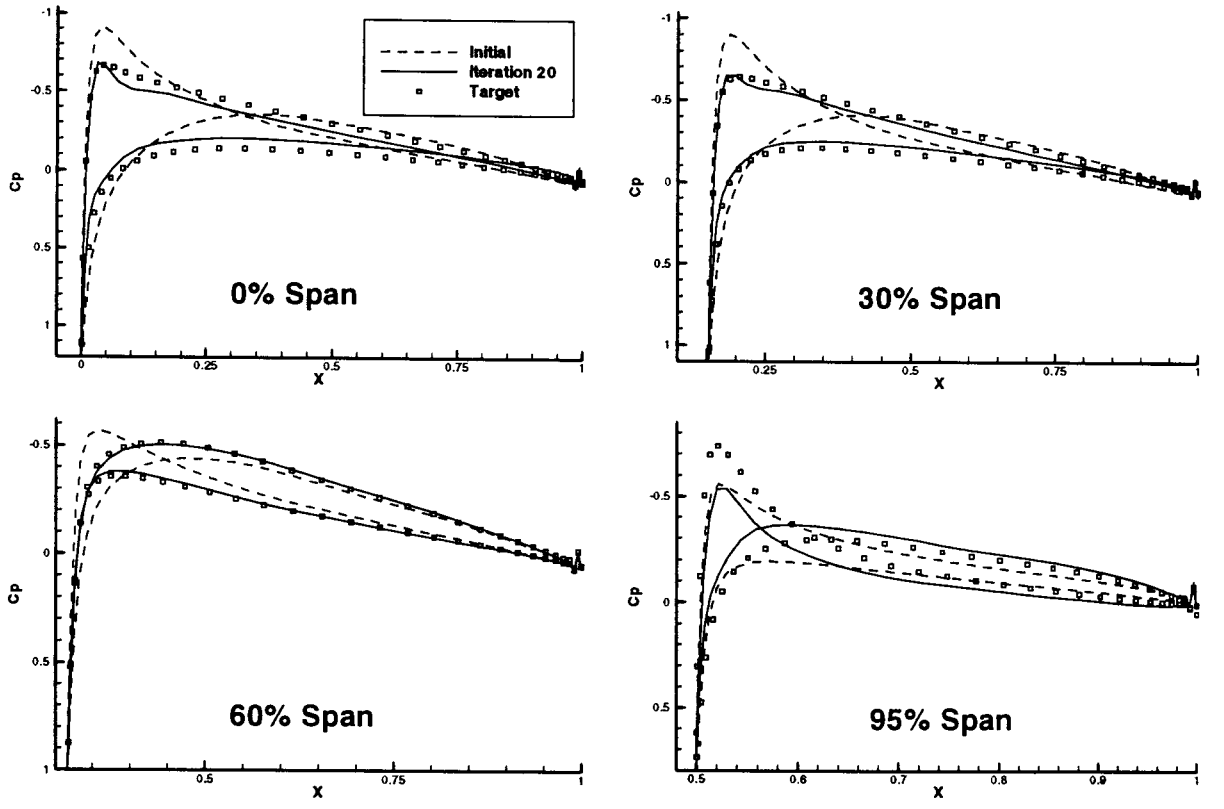

Fig. 13: Sectionwise Cp distributions for severely twisted Navier-Stokes subsonic case.

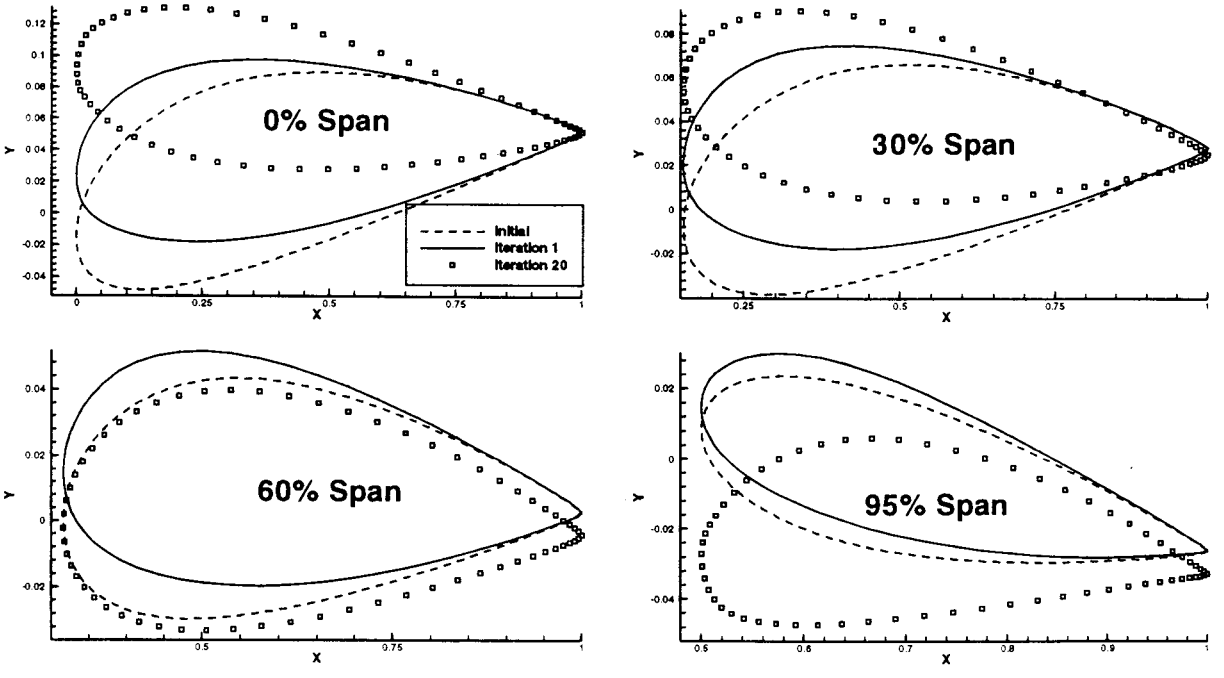

Fig. 14: Geometry evolution by section for severely twisted Navier-Stokes subsonic case. Y-axis enlarged for clarity.

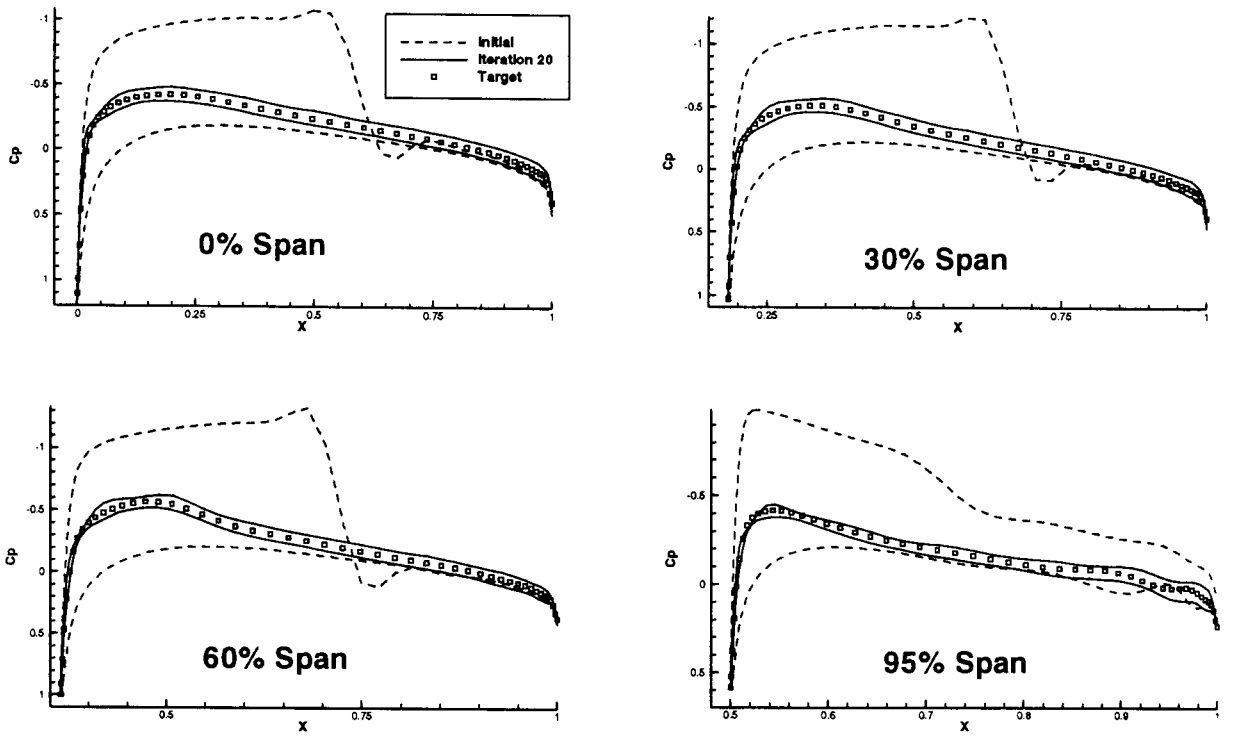

Fig. 15: Sectionwise Cp distributions for Euler shock removal case.

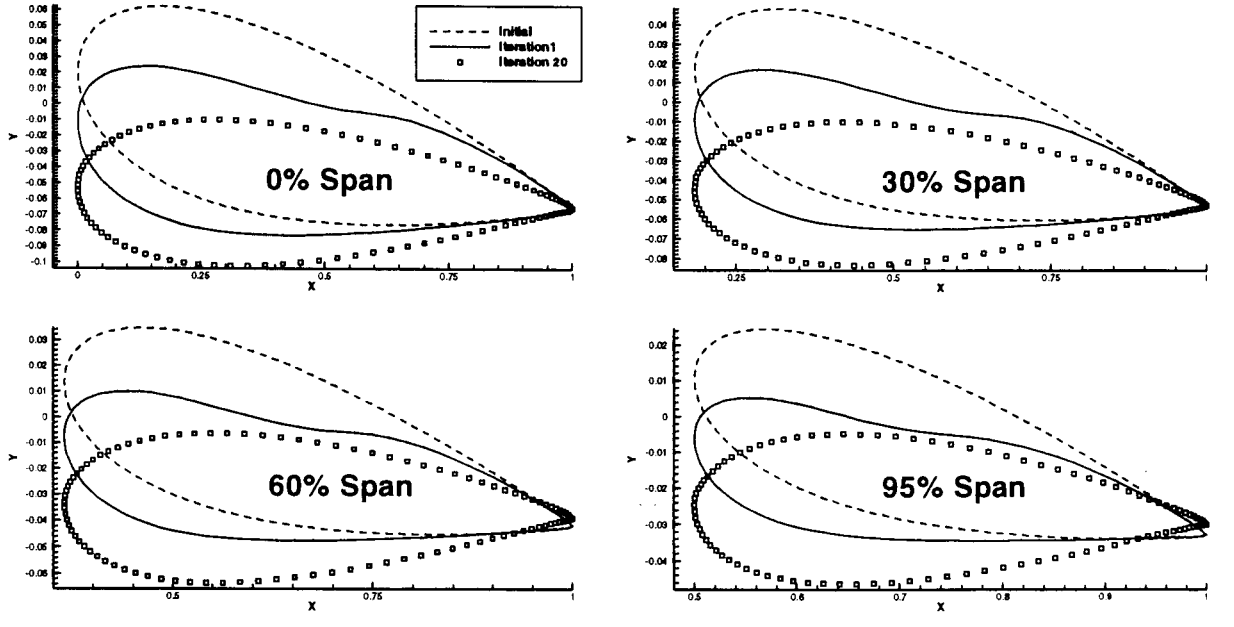

Fig. 16: Geometry evolution by section for Euler shock removal case. Y-axis enlarged for clarity

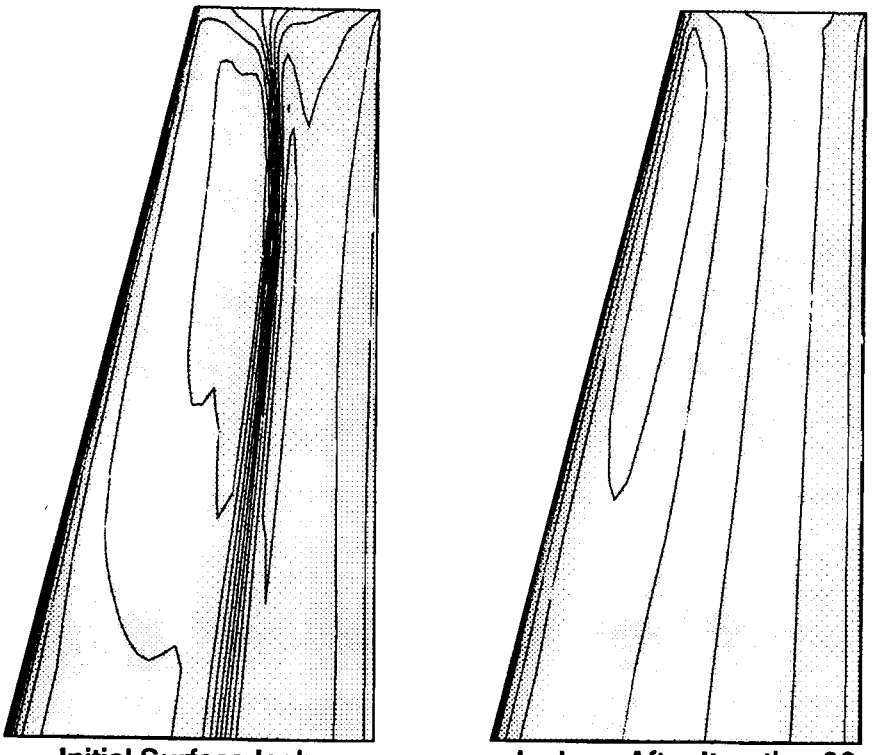

Fig. 17: Cp contours on upper side of wing for Euler shock removal case.